Nonlinear, Hybrid, Multicore Magnetic Energy Harvesting

Daniel Monagle, *Graduate Student Member, IEEE*, and Steven B. Leeb, *Fellow, IEEE*

***Abstract*—Current transformer magnetic energy harvesters scavenge energy from the magnetic fields around ac transmission lines to power sensor packages. Often, magnetic cores with either extremely high permeability (nanocrystalline alloys) or extremely high saturation flux density (silicon steel) are employed to make these harvesters. Although both high permeability and high saturation flux density are theoretically desirable for a magnetic energy harvester, a practical demonstration of a multimaterial harvester core that leverages the benefits of both high permeability and high saturation flux density core materials has yet to be shown. This article presents analysis and experimental demonstration of a multimaterial multicore magnetic energy harvester that is constructed from concentric toroids of different magnetic materials. Nonlinear flux models for this "hybrid" multicore energy harvester are presented and validated. The power harvest of the hybrid core is evaluated in comparison to traditional nanocrystalline and silicon steel harvesters and a critical result is shown. While the traditional nanocrystalline and silicon steel harvesters drastically outperform each other depending on the amplitude of the ac transmission line current, the hybrid core exhibits a high average power harvest over the entire range of transmission line current amplitudes, exploiting the high permeability of its nanocrystalline material at low currents and the high saturation flux density of its silicon steel material at high currents.**

***Index Terms*—Current transformer, hybrid core, magnetic core, magnetic energy harvesting, nonlinear, saturation, split-core.**

I. Introduction

ENERGY harvesting systems elude battery power supplies by scavenging energy from their surrounding environment. Advancing beyond battery-powered sensors is critical for the widespread deployment of Internet of Things (IoT) sensing devices and wireless sensing networks, as it is costly and impractical to periodically replace or recharge the batteries of millions or billions of individual sensor units. Energy harvesters act as transducers, scavenging and converting energy from the harvester installation environment in forms, such as solar [1], wind [2], vibration [3], or magnetic fields [4] into electrical energy for powering some device, such as a sensor package. Industrial infrastructure, such as manufacturing plant equipment or utility grid transmission lines, is especially suited for magnetic energy harvesting. This is because these settings are rich with conductors carrying ac current, from which magnetic energy harvesters can leverage Faraday's Law to scavenge energy from the time-varying magnetic fields around these conductors. Current transformer magnetic energy harvesters (CTMEHs), generally, clamp around a single turn of an ac current-carrying conductor, and harvested energy is delivered to the load (e.g., sensor package) connected to the secondary winding of the CTMEH.

Experimental demonstrations in the CTMEH literature often use either very high permeability nanocrystalline alloy cores, or very high saturation flux density silicon steel cores. Both high permeability and high saturation flux density are desirable material properties for magnetic energy harvesters [4]. Since magnetic energy harvesters exhibit maximum power harvest when driven to a certain degree of core saturation [4], [5], [6], [7], high permeability is desirable to promote a strong enough inductive coupling to drive the core into saturation [4]. High saturation flux density is also desirable because maximum attainable power harvest for a given core is directly proportional to the core's saturation flux density [4].

A significant body of existing literature has explored energy harvest enhancement strategies for magnetic energy harvesters. Strategies included methods that employ power electronic circuits with active switches to manipulate the saturation time or loading of the harvester core secondary winding [8], [9], active switches to de-saturate the core and enable multiple power harvest transfer windows per line cycle [10], actively-driven de-saturation control coils [11], and passive capacitive circuits for shaping the core flux [8] or resonating with the core magnetizing inductance [12]. While these enhancement circuits and control methods are indispensable for maximizing the power density of a given harvester core, existing literature that explores novel harvester core configurations or designs is relatively sparse.

Our previous work modeled and demonstrated the nonlinear power harvest of split nanocrystalline toroidal core CTMEHs [6]. The splitting of the core enabled nonintrusive installation of the harvester compared to an ungapped core, but the split core demanded new modeling techniques and exhibited lower power harvest than ungapped nanocrystalline cores. A few existing works have investigated the concept of using multiple cores in a single harvester assembly [5], [13], [14], [15]. Gao et al. [5] cascaded a split core, for easy installation, with a high permeability ungapped core, which features large shunt impedance and manageable saturation behavior for maximizing

Received 20 May 2025; revised 4 August 2025 and 28 August 2025; accepted 5 September 2025. Date of publication 9 September 2025; date of current version 23 December 2025. This work was supported by the Office of Naval Research Structural Acoustics Program. Recommended for publication by Associate Editor S. Jeong.*(Corresponding author: Daniel Monagle.)*

The authors are with the Department of Electrical Engineering and Computer Science, Massachusetts Institute of Technology, Cambridge, MA 02139 USA (e-mail: monagled@mit.edu; sbleeb@mit.edu).

Color versions of one or more figures in this article are available at https://doi.org/10.1109/TPEL.2025.3607641.

Digital Object Identifier 10.1109/TPEL.2025.3607641

power harvest. Liu et al. [13] proposed a dual-core structure of toroidal cores installed next to each other on a transmission line, where one core is used for harvesting and the other for sensing. Paul et al. [14] presented a dual-core structure of concentric, split toroidal cores of different magnetic materials. In addition, Paul et al. [14] demonstrated finite element analysis of the concentric core structure, with a focus on induced voltage in the secondary winding and the effects of different air gap geometries. Wang et al. [15] also explored various configurations of multimaterial energy harvesters, where the multicore harvester, which is also configured with two cores side by side along the ac transmission line, is twice the volume of core material than the single core harvesters used in that work. Minimum startup currents for a given harvester load and acceptable "working ranges" of transmission line primary wire current were studied in [15], but detailed nonlinear power harvest models that capture the continuous, saturation behavior of the harvester cores were not derived or demonstrated.

This article presents novel analysis and experimental demonstration of multimaterial CTMEHs assembled with concentric toroids of different core materials. Distinct from [6], where single-material split core harvesters were modeled and validated in the <10 A_{rms} current range, this article derives and validates nonlinear flux models for a heterogeneous, multimaterial harvester over a wide range of primary currents. The nonlinear flux modeling is implemented in SPICE and is experimentally validated for a multicore structure consisting of a split silicon steel (si-steel) magnetic core nested within a split nanocrystalline magnetic core.

The magnetic energy harvesting literature features harvesters evaluated at primary currents less than about 10 A_{rms} [4], [5], [6], [8], [10], [12], [16] and as high as several hundreds of rms amperes [7], [17], [18], [19]. The "low" current harvesters are often demonstrated with nanocrystalline alloy cores, whereas the harvesters demonstrated at "high" currents are typically si-steel. This article presents the "hybrid" core magnetic energy harvester, that leverages the high permeability of nanocrystalline and the high saturation flux density of si-steel to achieve high power harvests over a wide range of transmission line currents. The key contributions and revelations of this article are summarized as follows.

1) A multicore, hybrid magnetic energy harvester exhibits a greater maximum average power harvest than purely nanocrystalline or si-steel harvesters over a wide range of transmission line primary currents.
2) Nonlinear flux models, which capture the unsaturated, soft saturated, and hard saturated regimes of harvester operation, are proposed and validated for the hybrid magnetic energy harvester.
3) At a low 2.5 A_{rms} primary current, the hybrid core and the purely nanocrystalline core exhibit similar maximum average power harvest, while the si-steel core performs poorly.
4) At a high 30.0 A_{rms} primary current, the hybrid core and the purely si-steel core exhibit similar maximum power harvest, while the nanocrystalline core performs poorly.

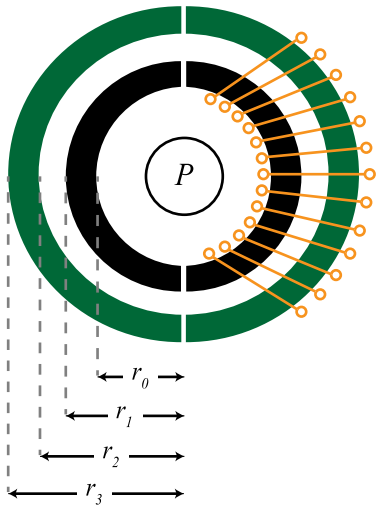

Fig. 1. Illustration of the hybrid harvester. The concentric toroids are each split cores that are clamped together around a primary wire (denoted P). A secondary winding wraps from the outer radius of the outer toroid to the inner radius of the inner toroid.

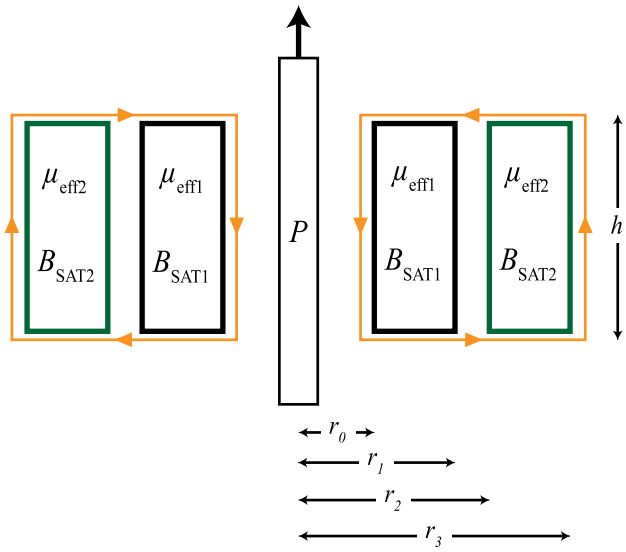

Fig. 2. Cross-sectional illustration of the hybrid harvester. Each winding turn surrounds both core materials.

5) The maximum average power harvest of a current transformer magnetic energy harvester, generally, does not scale linearly with primary current level over a wide primary current range.

II. Hybrid Core Analysis

This section presents the foundational modeling for describing the saturating behavior of a hybrid, multicore, multimaterial magnetic energy harvester, which is constructed from concentric toroids. Analytical formula are derived according to Maxwell's equations. An illustration of this proposed hybrid core harvester is shown in Fig. 1. A cross-sectional diagram of the hybrid core harvester is shown in Fig. 2. The harvester consists of an inner

split core of one material, shown in black in Fig. 1, and an outer split core of a different material, shown in green in Fig. 1. The air gaps at the mating surfaces of each semi-toroid have been exaggerated in Fig. 1 for illustration, but will be on the order of microns once the harvester halves are tightly clamped together around a primary wire during installation. The N-turn secondary winding wraps from the inner radius r_0 of the inner core to the outer radius of the outer core r_3. This yields, as shown in Fig. 2, a winding area that encompasses an inhomogeneous cross section: An inner toroid cross section with effective initial relative permeability μ_{eff1} and saturation flux density B_{SAT1}, an outer toroid cross section with effective initial relative permeability μ_{eff2} and saturation flux density B_{SAT2}, and some air between them.

The average power harvest of any magnetic energy harvester is a function of the amount of flux linked to the secondary winding per cycle of primary current. Thus, it is imperative that a designer be equipped with an accurate model of the flux linkage and an intuition for the effect of key magnetic material properties, such as effective initial relative permeability μ_{eff} and saturation flux density B_{SAT} on power harvest.

A. Hybrid Flux Derivation

Although our proposed hybrid harvester is built with 3 material regions (inner core, outer core, and air) for practical reasons, this analysis generalizes to n-materials, provided that the harvester dimensions are not so large or far away from the primary wire that fringing fields and excessive leakage become dominant factors. By definition, the total flux linkage of an N-turn secondary coil is

$$\Lambda(t) = N\Phi(t) \tag{1}$$

where $\Phi(t)$ is the flux through the cross-sectional area of a single winding in the secondary. Expressing (1) in terms of flux density $B(t)$ and the winding cross-sectional surface S gives

$$\Lambda(t) = N \int_S \vec{B}(t) \cdot d\vec{A}. \tag{2}$$

With reference to the cross-sectional diagram of Fig. 2, this analysis assumes that the flux density does not vary along the vertical axis, but only varies significantly between layers of different core materials. Thus, the core height h can be extracted from the surface integral. The total flux linkage can be re-written as

$$\Lambda(t) = N\,h \int_{r_0}^{r_n} \vec{B}(t) \cdot d\vec{r} \tag{3}$$

where r_0 is the innermost radius of the innermost core material and r_n is the outermost radius of the outermost core material from a primary wire origin depicted in Fig. 2.

For hybrid, multimaterial cores of n materials the total flux linkage is, therefore,

$$\Lambda(t) = N\,h \left[\int_{r_0}^{r_1} \vec{B}_1(t) \cdot d\vec{r} + \int_{r_1}^{r_2} \vec{B}_2(t) \cdot d\vec{r} + \dots + \int_{r_{n-1}}^{r_n} \vec{B}_n(t) \cdot d\vec{r} \right]. \tag{4}$$

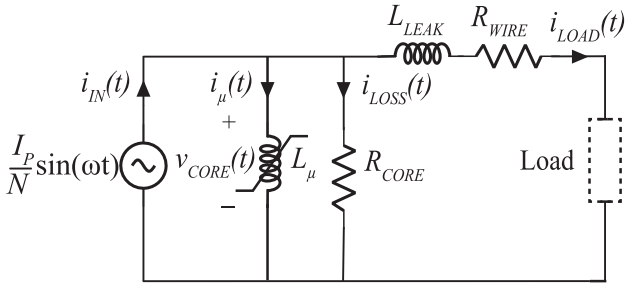

Fig. 3. Circuit model of CTMEH, in which a single lumped inductance can model behavior of the hybrid core.

This expression for total flux linkage of a CTMEH constructed from n concentric layers of different core materials is characterized by a sum of n individual flux density expressions, specific to each core material. An exciting feature of this derivation is that the total flux linkage through this complex, hybrid structure can be expressed with one single equation. Therefore, a single nonideal inductance can be used to model the behavior of this hybrid structure. An LTSPICE abritrary inductor model, for example, can support this total flux equation, where each $B(t)$ term in the summation is a nonlinear function tailored to the specific core material along the total r_0 to r_n integration.

A secondary-side, lumped circuit model of this system is shown in Fig. 3, where L_μ is the single, nonlinear magnetizing inductance of the hybrid structure whose behavior is described by (4).

Input current $i_{\text{IN}}(t)$ is the sinusoidal primary current divided by the turns ratio of the current transformer. R_{CORE} is an equivalent resistance to capture the core losses of the harvester core. L_{LEAK} and R_{WIRE} are the leakage inductance and dc wire resistance of the N-turn secondary winding, respectively. A generic "Load" is shown connected across the secondary winding.

For our proposed hybrid core shown above, the total n-term flux linkage summation of (4) reduces to three terms: One for the inner toroid ($\vec{B}_{\text{IN}}(t)$), one for the air between the inner and outer toroid ($\vec{B}_{\text{AIR}}(t)$), and one for the outer toroid ($\vec{B}_{\text{OUT}}(t)$)

$$\Lambda(t) = N\,h \left[\int_{r_0}^{r_1} \vec{B}_{\text{IN}}(t) \cdot d\vec{r} + \int_{r_1}^{r_2} \vec{B}_{\text{AIR}}(t) \cdot d\vec{r} + \int_{r_2}^{r_3} \vec{B}_{\text{OUT}}(t) \cdot d\vec{r} \right]. \tag{5}$$

Assuming the magnetic flux density does not vary as a function r within the same core material, we have

$$\Lambda(t) = N\,h\,[(r_1 - r_0)\,B_{\text{IN}}(t) + (r_2 - r_1)\,B_{\text{AIR}}(t) + (r_3 - r_2)B_{\text{OUT}}(t)]. \tag{6}$$

Here, a designer should choose an appropriate function for each $B(t)$ term in the hybrid core construction. This choice of $B(t)$ for each term in the total flux linkage is itself a nontrivial process. Piecewise models that abruptly change effective permeability to μ_0 once the core is "saturated" offer simplicity, but such models fail to capture the gradual rolloff of $\partial B/\partial H$ exhibited in soft saturation between the unsaturated linear regime and hard saturation. Soft saturation is of particular importance because CTMEHs exhibit maximum power harvest in the soft saturation regime [4], [6]. Generally, one of the family of "S-shaped" functions, sometimes referred to as "sigmoid" functions ($\arctan(x)$, $\tanh(x)$, $\mathrm{erf}(x)$ etc.), is a suitable choice for capturing the gradual saturation behavior, from unsaturated to soft saturated to hard saturated regimes, exhibited by magnetic cores. Just as the B–H curves of many magnetic materials, sigmoids exhibit a relatively constant slope near the origin and gradually rolloff to a constant value at large input arguments. To map a sigmoid to a physical flux density $B(t)$, one must define $B(t) = f(H(t))$, substitute $H(t) = Ni(t)/l$, and provide the appropriate scaling factors to ensure that the sigmoid $H(t)$ argument is scaled by some term capturing initial magnetic permeability and that the sigmoid converges to a material B_{SAT} at large H. In this article, we use $\arctan(x)$ and $\tanh(x)$ functions for describing the flux densities of the core materials, depending on the magnitude of the primary current. Broadly speaking, for the hybrid cores in this work, we have found hyperbolic tangent to yield strong agreement between experiment and simulation at low primary currents and arctangent to yield strong agreement at high primary currents. Specifically, our tanh models are

$$B_{\mathrm{IN}}(t) = B_{\mathrm{SAT1}} \tanh\left(\frac{N\, i_\mu(t)}{l_{\mathrm{IN}}} \frac{\mu_{\mathrm{eff1}}\mu_0}{B_{\mathrm{SAT1}}}\right) \tag{7}$$

$$B_{\mathrm{OUT}}(t) = B_{\mathrm{SAT2}} \tanh\left(\frac{N\, i_\mu(t)}{l_{\mathrm{OUT}}} \frac{\mu_{\mathrm{eff2}}\mu_0}{B_{\mathrm{SAT2}}}\right) \tag{8}$$

where l_{IN} is the mean magnetic flux path length of the inner toroid, l_{OUT} is the mean magnetic flux path length of the outer toroid, and $i_\mu(t)$ is the instantaneous magnetizing current flowing through the hybrid core equivalent nonlinear magnetizing inductance. Our arctan models are

$$B_{\mathrm{IN}}(t) = B_{\mathrm{SAT1}} \frac{2}{\pi} \arctan\left(\frac{\pi}{2} \frac{N\, i_\mu(t)}{l_{\mathrm{IN}}} \frac{\mu_{\mathrm{eff1}}\mu_0}{B_{\mathrm{SAT1}}}\right) \tag{9}$$

$$B_{\mathrm{OUT}}(t) = B_{\mathrm{SAT2}} \frac{2}{\pi} \arctan\left(\frac{\pi}{2} \frac{N\, i_\mu(t)}{l_{\mathrm{OUT}}} \frac{\mu_{\mathrm{eff2}}\mu_0}{B_{\mathrm{SAT2}}}\right) \tag{10}$$

where the $\frac{2}{\pi}$ normalizes the arctangent function to saturate at 1 (such that $B(t)$ saturates at B_{SAT}), and where the $\frac{\pi}{2}$ factor normalizes $\partial B(t)/\partial H(t)$ of the arctangent function to equal $\mu_{\mathrm{eff}}\,\mu_0$ when $H(t) = (N\, i_\mu(t)/l) = 0$. We use a linear B–H curve for describing the properties of the $B_{\mathrm{AIR}}(t)$ term

$$B_{\mathrm{AIR}}(t) = \mu_0 \frac{N\, i_\mu(t)}{l_{\mathrm{AIR}}} \tag{11}$$

where l_{AIR} is the mean magnetic flux path length of the air path between the inner and outer toroids. Since both the inner and outer cores are wrapped together with the same winding, the magnetizing current is shared between all $B(t)$ terms in the total flux linkage summation. It is important to note that these sigmoids alone do not capture core losses. The additional equivalent core loss resistance parameter, R_{CORE} of Fig. 3, is necessary to model the core losses of the harvester. As we show in our experimental validation, core losses are negligible for the hybrid harvester except under very low primary current excitations. For the most accurate modeling at low currents, a tandem of nonlinear sigmoids and an appropriate R_{CORE} is critical for modeling both magnetic saturation and losses.

Substituting the appropriate $B_{\mathrm{IN}}(t)$, $B_{\mathrm{OUT}}(t)$, and $B_{\mathrm{AIR}}(t)$ into (6) gives a single, nonlinear total flux linkage that captures the hybrid core behavior modeled in the circuit of Fig. 3. To implement such a model in SPICE, core geometry parameters, number of secondary turns, and magnetic material properties must be declared. Geometry and turn count are known to the designer or can be swept to inform a design process. The magnetic material properties, however, are relatively limited to those provided by commercial magnetic core manufacturers. Since the hybrid core harvesters explored in this article are split cores, further discussion regarding effective initial permeability and saturation flux density is warranted.

B. Magnetic Material Parameters

To use the flux model derived above, a designer must have candidate μ_{eff} and B_{SAT} material parameters for each core in the multicore assembly. Of course, a numerical sweep of these parameters could be performed to best fit the predictions of the circuit model presented above to experimental observations. A theoretical basis and intuition, however, for the effects of cutting and clamping the high-performing magnetic materials used in these harvesters is extremely valuable for a designer. Estimating the magnetic material parameters for simulation from theory provides great utility, as it permits a productive and accurate design process without the requirements to first obtain and experimentally characterize a specific set of magnetic cores.

B_{SAT} does not significantly vary between split and ungapped cores of the same material. Effective initial permeability, however, can change dramatically due to the core cutting process and the residual presence of extremely small surface roughness air gaps present at the mating surfaces of the semi toroids when the halves of the harvester are clamped together at installation [20], [21], [22]. Depending on the specific cutting process used, the surface roughness air gaps might range from about 1–6 microns for high precision laser cuts to 1–50 microns for less precise wire cuts [20]. An approximation for the effective initial relative permeability μ_{eff} of a core as a function of air gap length l_{gap} is given by [22]

$$\mu_{\mathrm{eff}} = \frac{\mu_{\mathrm{core}}}{1 + \left(\frac{l_{\mathrm{gap}}}{l_{\mathrm{flux}}}\right)\mu_{\mathrm{core}}} \tag{12}$$

where μ_{core} is the effective initial relative permeability of the core before cutting, and l_{flux} is the mean magnetic flux path length. Fig. 4 plots (12) for notional nanocrystalline and silicon steel cores. This plot illustrates a few key features of split cores and their modeling complications. First, micron surface roughness

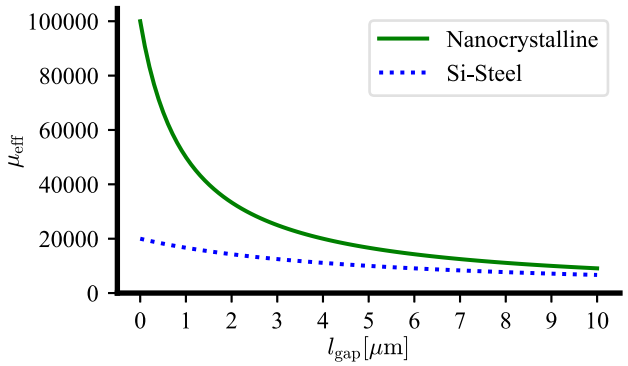

Fig. 4. Effect of surface roughness air gaps on different magnetic materials ($l_{\text{flux}} = 100$ mm, Nanocrystalline $\mu_{\text{core}} = 100\,000$, Si-Steel $\mu_{\text{core}} = 20\,000$).

gap lengths cause drastic reductions in μ_{eff}, especially for extremely high permeability nanocrystalline alloys. Second, this extreme sensitivity of μ_{eff} to l_{gap} is especially pronounced in the $(0, 5]$ μm range. Finally, the large difference in initial, ungapped μ_{core} of nanocrystalline and si-steel is quickly trounced once gap lengths of about 5 microns exist. Such analysis implies that a split hybrid harvester of these materials likely features a μ_{eff1} and μ_{eff2} related by a $2\times$ or $3\times$ factor, rather than a drastic $5\times$ or more factor that an ungapped hybrid harvester might exhibit. This theoretical basis, complemented by a knowledge of practical gap sizes left from core cutting techniques, serves as our method of estimating μ_{eff1} and μ_{eff2} in this article.

C. General Material Selection Criteria

A few key questions naturally follow for hybrid harvester designs. Namely, how does one select core materials and arrange their configuration as inner or outer cores to maximize power harvest? How should a designer think about the distinctions of arctangent versus hyperbolic tangent flux models? And what implications do variations in μ_{eff} have on modeling and resulting power harvest? This section explores these questions by presenting power harvest simulation results for a variety of harvester material arrangements. The nonlinear, multiterm flux description and equivalent circuit model presented in Section II-A were implemented in LTSPICE as a single nonlinear magnetizing inductance for several conceptual lossless, split, multicore harvester designs. One design consists of only nanocrystalline concentric split toroids. Another consists of only si-steel concentric split toroids. Finally, two multimaterial hybrid designs with different material ordering are also presented. One design, called "Hybrid 1", consists of an inner si-steel split toroid and an outer nanocrystalline split toroid. The final design, called "Hybrid 2" consists of an inner nanocrystalline split toroid and an outer si-steel split toroid. Across all harvester designs, each portion of nanocrystalline material was assumed to have $\mu_{\text{eff}} = 25000$ and $B_{\text{SAT}} = 1.2$T. Each portion of si-steel material was assumed to have $\mu_{\text{eff}} = 10000$ and $B_{\text{SAT}} = 2.0$T. Arctangent flux models were used for all harvesters. A summary of the harvester simulation parameters in SPICE is given in the Appendix.

In simulation, each harvester design was evaluated at a variety of 60 Hz sinusoidal primary current conditions with a resistive load connected to the secondary winding of the harvester. At each primary current, the resistive load was swept in LTSPICE, and the maximum average power harvest P_{MAX} for each notional harvester design was recorded. Fig. 5 displays the simulated P_{MAX} values over a very wide primary current range of 1.0–100.0A $_{\text{rms}}$. This plot sheds light on material selection considerations for designers. At small primary currents, coupling is king. At $I_P = 1.0$ A_{rms}, the nanocrystalline and Hybrid 2 designs outperform the Hybrid 1 and si-steel designs, with nanocrystalline and Hybrid 2 P_{MAX} values that are 237% and 182% respectively of the si-steel P_{MAX}. The highest overall effective permeability is given by a purely nanocrystalline design. Thus, it promotes the best coupling to the primary winding and exhibits the largest P_{MAX} under low current conditions. Although Hybrids 1 and 2 are both designed with nanocrystalline and si-steel material in a single harvester, the ordering of materials has a clear effect on performance. Hybrid 2's inner nanocrystalline split toroid features its higher μ_{eff} material over a shorter mean magnetic flux path length than the outer nanocrystalline split toroid of Hybrid 1. At low magnetic field excitations, the disparity between the relatively high μ_{eff1} inner nanocrystalline toroid of Hybrid 2 and relatively low μ_{eff1} inner si-steel toroid of Hybrid 1 yields better maximum power harvest for Hybrid 2. Alternatively, at large primary currents, materials with high saturation flux density perform best. The excitation field strengths are so large that transformer coupling is no longer a primary design concern. Rather, a higher ceiling of material B_{SAT} is advantageous so that a given core volume is capable of transferring more energy per line cycle before becoming undesirably hard saturated. Under these high current conditions, the purely si-steel design exhibits the most total material over which $B_{\text{SAT}} = 2.0$ T and therefore exhibits the largest P_{MAX}. At $I_P = 100.0$ A_{rms}, the P_{MAX} of si-steel and that of Hybrid 1 are respectively 148% and 126% that of nanocrystalline. While the nanocrystalline design lags deeply behind, the performance of Hybrids 1 and 2 converges as coupling, and therefore the inner vs outer ordering of the si-steel and nanocrystalline portions matters less, and the saturation flux density matters more. At the $I_P = 15.0$ A_{rms} operating point, a "medium" current level, we observe the interesting result that Hybrid 2 shows the lowest P_{MAX} of the 4 designs. Hybrid 1, the purely si-steel, and the purely nanocrystalline CTMEHs assume first, second, and third place respectively. This ranking is again explained through a story of coupling. The "leading" designs, Hybrid 1 and si-steel, share the feature of having a lower μ_{eff}, higher B_{SAT} material over a shorter mean magnetic flux path length of the inner toroid. The shorter magnetic flux path length compensates for the lower μ_{eff} material to yield overall magnetic reluctance that is small enough for considerable flux to flow through the inner si-steel toroid portions and capitalize on the higher B_{SAT} ceiling. At "medium" primary currents, the extra B_{SAT} of si-steel material is only taken advantage of if the total reluctance of the si-steel path is low enough to channel significant magnetic flux. Since Hybrid 2's high B_{SAT} si-steel portion is arranged over the long magnetic flux path of its outer toroid, its si-steel portion is underutilized as that path's reluctance is still too large for the 15.0A_{rms} primary current condition to push substantial flux through the outer toroid

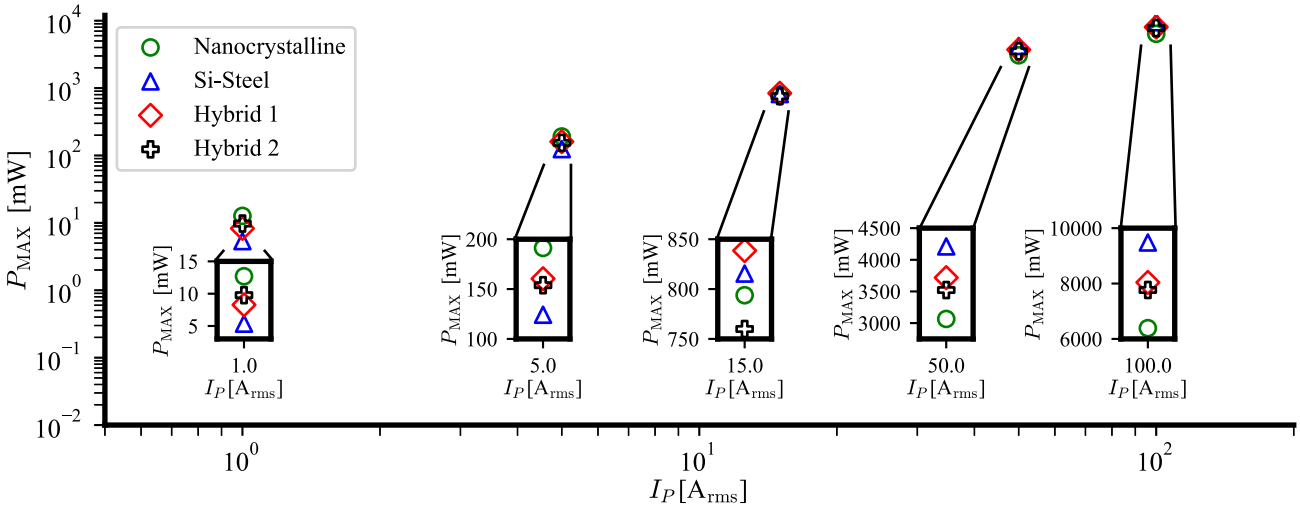

Fig. 5. SPICE-simulated power harvest data shows that the optimal harvester material choices vary with primary current operating point.

and exploit the higher B_{SAT}. While the purely nanocrystalline design has no 2.0T material at all, it still outperforms Hybrid 2 at this primary current condition because the purely nanocrystalline design's outer toroid is relatively high μ_{eff}, presenting a comparatively appealing flux path for the magnetic fields and coupling more energy through the overall winding area of the harvester.

Throughout the entire primary current range, the hybrid designs are competitive with the nanocrystalline and si-steel designs. At the $I_P = 15.0$ A$_{\mathrm{rms}}$ operating point within the primary current range, we emphasize that Hybrid 1 actually outperforms both the purely nanocrystalline and si-steel designs, with a Hybrid 1 P_{MAX} that is 106% that of nanocrystalline and 103% that of si-steel. This exciting result suggests that, compared to conventional, single-material designs, a hybrid harvester can exhibit the best maximum power harvest around a nominal primary current operating point, and also maintain strong performance over a wide range of primary current amplitude variations.

For any one harvester design, the choice of nonlinear sigmoid function for saturation flux modeling has a notable affect on predicted power harvest. One can compare the outcomes of the arctangent and hyperbolic tangent flux models to highlight their key differences in informing the design process. Fig. 6 shows the LTSPICE-simulated average power harvest P_{LOAD} for the Hybrid 1 harvester across secondary load resistance R_{LOAD} sweeps under low 2.5A$_{\mathrm{rms}}$ and high 25.0A$_{\mathrm{rms}}$ primary current excitations. Simulation results are overlaid for one sweep where arctangent flux models were used and another sweep, where hyperbolic tangent flux models were used. We see, as expected, that the models predict virtually equivalent power harvest in the linear, unsaturated regime, where the distinctions between the arctangent and hyperbolic tangent functions are negligible. The models begin to diverge in power harvest predictions, however, as the core enters soft saturation where maximum power harvest occurs. They continue to maintain a nonnegligible difference deeper into hard saturation at large R_{LOAD}. The comparisons of Fig. 6 capture a useful insight for a hybrid core designer. First, at both low and high primary

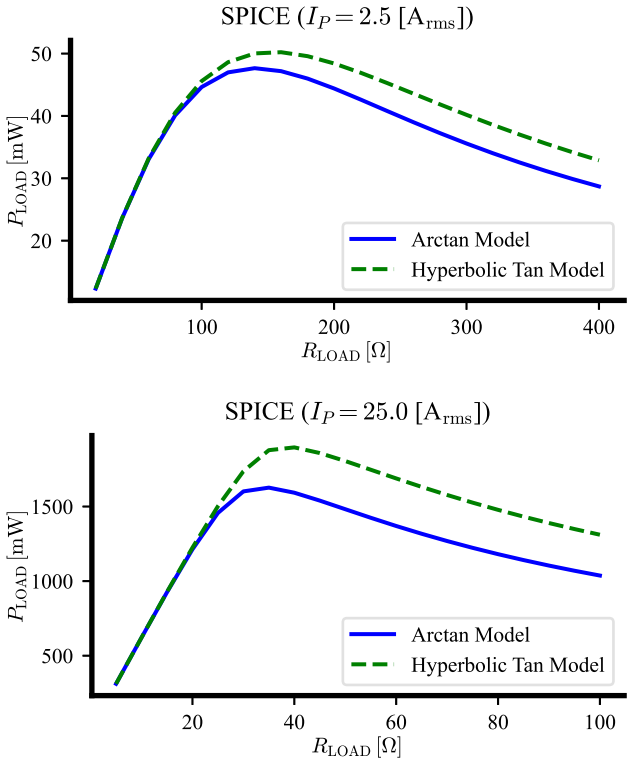

Fig. 6. Arctangent flux modeling provides a conservative estimate of average power harvest compared to hyperbolic tangent.

currents, the hyperbolic tangent model overpredicts the average power harvest predicted by the arctangent model. Second, the discrepancy between these sigmoid models grows larger under higher primary current conditions. For example, the maximum power harvest of the hyperbolic tangent models is only 105% that of the arctangent models at $I_P = 2.5$ A$_{\mathrm{rms}}$, but is 117% that of the arctagnent models at $I_P = 25.0$ A$_{\mathrm{rms}}$. The key takeaway is that, for equivalent geometries and magnetic material parameters, arctangent provides a more conservative power harvest estimate than hyberbolic tangent. This feature of two otherwise very

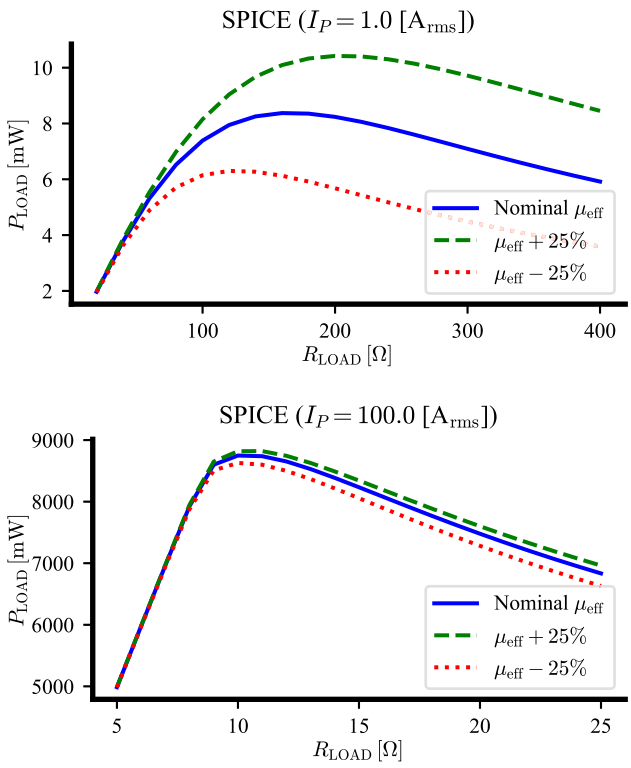

Fig. 7. Effective initial permeability variation has a significant effect on power harvest at low primary currents, but very little noticeable effect at high primary currents.

similar sigmoid functions can be leveraged by a designer, for example, to produce a conservative, first pass harvester design with arctangent accompanied by a more aggressive design with hyperbolic tangent. As we will show in Fig. 11 and discuss in Section III, one sigmoid choice may more accurately capture the exact minor magnetization loop traversal of an experimental CTMEH. Depending on the specific core materials used, secondary loading, and primary current operating conditions, one model or a completely different sigmoid may yield the best agreement with experimental data, but this $\arctan(x)$ versus $\tanh(x)$ comparison provides a sound basis upon which further modeling refinements can be made.

Finally, as demonstrated by the simulation results of Fig 5, effective initial relative permeability is critical in determining power harvest performance, especially at lower primary currents. μ_{eff}, however, can notoriously vary due to a variety of factors, including the peak amplitude of the excitation signal [23], [24], the temperature [25], [26], or the core cutting process and residual surface roughness discussed in Section II-B. Fig. 7 shows a set of LTSPICE-simulated average power harvest curves over a secondary resistive load sweep for the Hybrid 1 harvester, assuming hyperbolic tangent flux modeling. Simulations were run at 1.0 A_{rms} and 100.0A_{rms} 60 Hz sinusoidal primary currents, and power harvest curves are shown for the nominal $\mu_{eff1} = 25\,000$ and $\mu_{eff2} = 10\,000$ parameter values alongside $\pm 25\%$ variations in both effective initial relative permeability parameters. Consistent with the coupling discussion illustrated by the power harvest data of Fig. 5, once again we see that Fig. 7 highlights the drastic effects of effective permeability at low current excitations compared to the relatively negligible effects at high current excitations.

TABLE I
CORE GEOMETRIES (ALL HARVESTERS)

r_0 [mm]	r_1 [mm]	r_2 [mm]	r_3 [mm]	h [mm]
9	14	16	21	20

This simulation results and discussion of this section serve to inform a designer about the relative merits of CTMEH material properties and modeling approximations on power harvest performance. These results emphasize that high effective permeability is a critical design target at low primary currents, while saturation flux density is essential to strong performance at high primary currents. In the low current operating regime, the order of which materials assume the positions of inner and toroids has a notable affect on power harvest. The performance of hybrid cores with different ordering of inner and outer core materials, however, converges as primary current excitations grow very large. Furthermore, effective permeability variations can have serious consequences for design and performance at low primary currents, but have little effect on power harvest modeling at high primary currents. This intuition regarding which material parameters matter most at which operating conditions is extremely useful for orienting the CTMEH design process to meet harvester load power budgets.

III. EXPERIMENTAL VALIDATION

Three harvesters were assembled in order to compare the performance of the novel hybrid core with that of single-material cores. All cores were obtained from CoilCore (Guangzhou Amorphous Electronic Technology Company, Ltd. [27]) in the desired materials and geometry at the request of the authors' of this article. Each harvester assembly consists of two, toroidal, concentric, split magnetic cores of identical geometries, around which one, 100-turn secondary winding is wound around the entire concentric structure as shown in Fig. 1. The inner split core and the outer split core each consist of two semi-toroids. Each 100-turn winding is hand-wound on one half of the total harvester assembly, where 2 layers of about 50 turns each are approximately evenly distributed over the entire half-arc of the harvester. The identical geometry ensures a fair comparison between harvesters. One harvester consists of exclusively nanocrystalline concentric toroid cores. The next harvester consists of exclusively si-steel concentric toroids. The novel hybrid harvester consists of an inner si-steel core and an outer nanocrystalline core. The uninstalled harvester assemblies are shown in Fig. 8.

Each harvester is later clamped around a primary wire for harvester installation and experimentation. The core dimensions are included in Table I.

Using standard C-clamps, each harvester was tightly clamped around a single turn of primary wire, and a variable resistive load, R_{LOAD}, was connected across the secondary winding of the harvester under test. A KEPCO BOP-MG power supply was

Fig. 8. Uninstalled harvester assemblies with US 1 Dollar bill for size reference. (Left to right: Nanocrystalline, Silicon-Steel, Hybrid.)

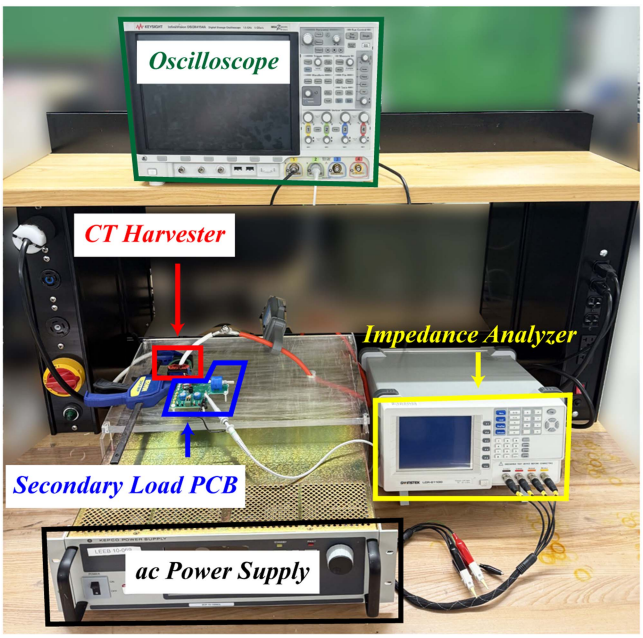

Fig. 9. Annotated photograph of energy harvesting experimental setup.

configured to provide a 60-Hz ac current through the primary wire, from which the harvester under test scavenged energy. Tests were performed for each harvester (Nanocrystalline, Si-Steel, Hybrid) under primary current (I_P) conditions of 2.5A_{rms}, 5.0A_{rms}, 10.0A_{rms}, 20.0A_{rms}, and 30.0A_{rms}. At each I_P condition, the resistive load on the secondary winding was swept over a wide range, subjecting the harvester to varying levels of saturation. Average power harvest P_{LOAD} was obtained from directly measuring the rms voltage across the resistive load on the secondary winding, squaring it, and dividing by the load resistance on the secondary winding. A Keysight InfiniiVision DSOX4154A oscillosocpe was used for this secondary winding voltage measurement, where the rms measurement was directly calculated using the oscilloscope's measurement functionality. Each R_{LOAD} condition on the secondary winding was measured with a GW-INSTEK LCR-8110G precision LCR meter. A photograph of the experimental setup is shown in Fig. 9.

Fig. 10 displays the experimental maximum average power harvest P_{MAX} of each harvester assembly at each 60 Hz rms primary current level. This plot highlights several key contributions of this work and of the proposed hybrid core harvester.

TABLE II
HYBRID SPICE SIMULATION MATERIAL PARAMETERS

μ_{eff1} [unitless]	B_{SAT1} [T]	μ_{eff2} [unitless]	B_{SAT2} [T]
$10000 \pm 10\%$	2.0	$25000 \pm 10\%$	1.2

At relatively low primary currents (2.5 A_{rms}), the power harvest of the nanocrystalline core significantly outperforms that of the si-steel core. This is because the higher μ_{eff} of the nanocrystalline core promotes a stronger coupling to the primary winding and presents a larger magnetizing inductance impedance than the lower μ_{eff} si-steel harvester. The driving H-field at these low primary currents is so small that the extra headroom of B_{SAT} provided by a si-steel core is rendered effectively useless. As the primary current excitation increases, the P_{MAX} of the si-steel core grows more competitive with that of nanocrystalline. Under relatively high I_P conditions (20.0A_{rms} and 30.0A_{rms}) the importance of high μ_{eff} is trounced as saturation flux density becomes the dominant core material parameter for maximum average power harvest.

Meanwhile, the hybrid core exhibits competitive P_{MAX} over the entire 2.5–30.0A_{rms} primary current range. Through the center region of this range (5.0A_{rms}, 10.0A_{rms}, and 20.0A_{rms}) the hybrid core demonstrates the highest maximum average power harvest compared to either of the single-material harvesters. At $I_P = 10.0\ A_{rms}$, the hybrid core P_{MAX} of 501.36 mW notably exceeds that of si-steel (409.29 mW) and nanocrystalline (421.38 mW). These results demonstrate the exciting result that a hybrid core is especially apt for magnetic energy harvester applications in which the rms current level of the primary wire varies widely during operation.

Another interesting feature of Fig. 10 is that, for any harvester, P_{MAX} does not generally scale linearly with I_P over this wide I_P range. The low μ_{eff}, high B_{SAT} si-steel harvester, for example, seems to exhibit a P_{MAX} that scales roughly with ${I_P}^2$ from the 2.5–5.0A_{rms} test. As I_P is increased, however, this same harvester's P_{MAX} exhibits a diminishing return with increasing I_P, scaling somewhere between quadratically and linearly with I_P at higher currents. The nanocrystalline and hybrid core also exhibit diminishing P_{MAX} scaling with I_P that is greater than linear but less than quadratic over this wide primary current range.

Of course, the average power harvest delivered to the resistive load on the core secondary also varies dramatically for each harvester as a function of R_{LOAD}, since the R_{LOAD} connected to the core secondary has a significant effect on the saturation behavior of the harvester. Fig. 11 displays the experimental P_{LOAD} of the three harvester assemblies as a function of the resistive load value on the harvester secondary winding for each primary current test condition. The circuit model of Fig. 3 was implemented in LTSPICE, and the experimental data are overlaid with a solid curve of SPICE-simulation predicted average power harvest for the hybrid core. The SPICE simulation was implemented using a single, nonlinear magnetizing inductance whose flux description was given as a sum of three flux density terms as described in Section II-A. The magnetic material parameters for the hybrid core SPICE simulation are recorded in Table II, where the μ_{eff} terms were informed by the surface roughness gap length discussion presented in Section II-B of this article.

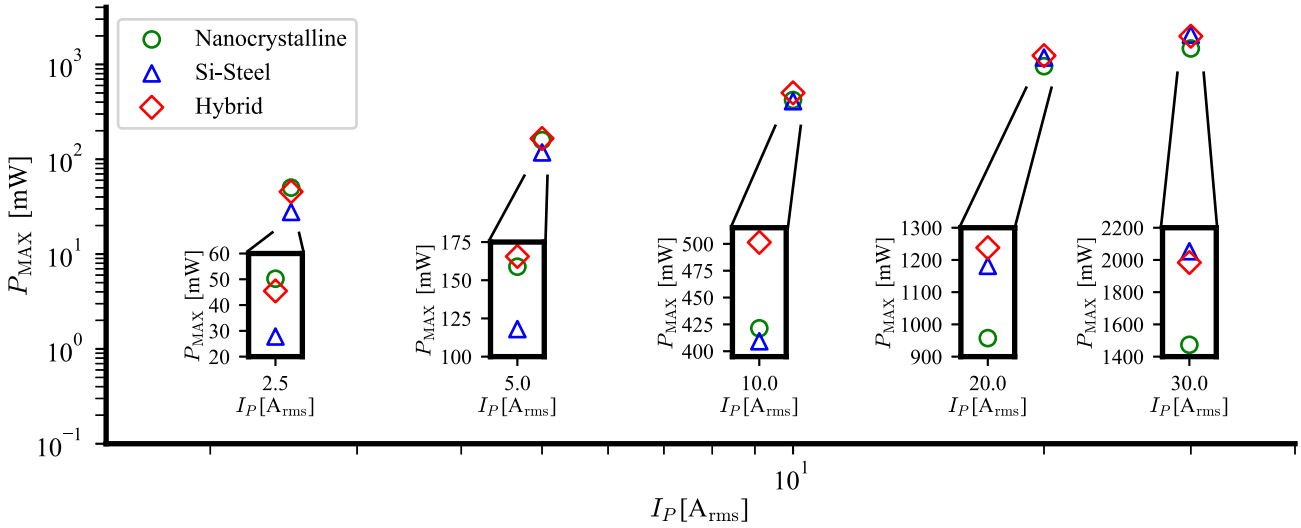

Fig. 10. Experimental comparison of maximum average power harvest between the Nanocrystalline, Si-Steel, and Hybrid harvesters over a wide range of primary currents highlights the consistently strong performance of the Hybrid core.

For each I_P and R_{LOAD}, the harvester traverses a unique B–H loop with slight variations in permeability and overall shape. For each I_P test, distinct μ_{eff} simulation parameters were selected within the $\pm 10\%$ tolerances from their nominal values of 10 000 and 25 000 to yield strong fits with experimental data. Similarly, as discussed in Section II, the appropriate sigmoids for the core material $B(t)$ terms (arctangent or hyperbolic tangent) were also chosen accordingly to yield a strong fit with experimental data at each I_P test. Thus, hyperbolic tangent models were used for the inner and outer toroid flux descriptions in simulation for the 2.5A$_{\text{rms}}$, 5.0A$_{\text{rms}}$, and 10.0A$_{\text{rms}}$ tests, and arctangent models were used for validation with the 20.0A$_{\text{rms}}$ and 30.0A$_{\text{rms}}$ tests. For illustrative purposes, the 30.0A$_{\text{rms}}$ plot includes hybrid core SPICE simulation results for both the arctangent and hyperbolic tangent models (using the same magnetic material simulation parameters). The overlaid SPICE and experimental data curves emphasize the overestimated P_{LOAD} of the hyperbolic tangent model compared to the experimental data, which is more accurately captured by the arctangent model. To avoid overcrowding of the other primary current datasets, only either the arctangent or hyperbolic tangent model is shown for each other I_P test based on which showed stronger agreement with the experimental data. Core loss was not modeled in this set of simulated data, but will be explored further in the next subsection. Secondary winding wire resistance and leakage inductance were ignored.

Every dataset exhibits a maximum average power harvest $P_{\text{LOAD}} = P_{\text{MAX}}$ in the nonlinear soft saturation regime, and average power harvest eventually decreases as each harvester is driven into deeper saturation at larger R_{LOAD} values. With respect to the circuit model of Fig. 3, as the core is driven into deeper saturation, the CTMEH magnetizing inductance acts, such as a short circuit for a greater portion of the input line cycle, shunting secondary current away from the load and causing overall lower power harvest. These power harvest characteristics are consistent with existing literature [4], [6], [17]. The resulting SPICE-simulated P_{LOAD} curve agrees well with the experimental power harvest of the hybrid core for most of the experimental data, but a discrepancy between the simulated and experimental power harvest arises in the very low primary current dataset, $I_P = 2.5\,\text{A}_{\text{rms}}$. This is likely due to the neglect of core loss in the above modeling and slight errors in magnetic material parameter estimation, which as discussed in Section II-B, is especially sensitive for split cores. The next section presents updated SPICE modeling that includes nonzero core loss and effective initial permeability refinements that correct for this discrepancy.

A. Loss Correction

Under low current excitations, the harvester cores traverse a minor magnetization loop exhibiting some core loss and changing effective permeability from a nominal value. As stated above, the SPICE-simulated power data presented in Fig. 11, assumed nominal μ_{eff1} and μ_{eff2} of 10 000 $\pm 10\%$ and 25 000 $\pm 10\%$ for the inner si-steel core and outer nanocrystalline core, respectively. These choices were informed from the theoretical effective initial permeability reduction presented in Section II-B for micron gap lengths associated with standard core cutting techniques. The SPICE-simulated data presented in Fig. 11 demonstrates strong agreement despite assuming zero core loss, which warranted its presentation to emphasize how accurate the modeling is even when simplified. More precisely, however, some nonzero core loss must be present, and the nominal permeability estimates likely slightly differ from the actual permeabilities of the experimental cores, given the high sensitivity of permeability to small, surface roughness gap lengths. Accounting for core loss is also especially important at low primary current levels, as the core loss affects a greater percentage of the relatively small power harvest.

Fig. 12 overlays the 2.5 A$_{\text{rms}}$ hybrid core experimental data with several curves of SPICE-simulated power harvest data, in which loss was modeled using a lumped core loss resistance R_{CORE} (as shown in Fig. 3), and μ_{eff} estimates were varied. Specifically, simulations are shown for the existing lossless

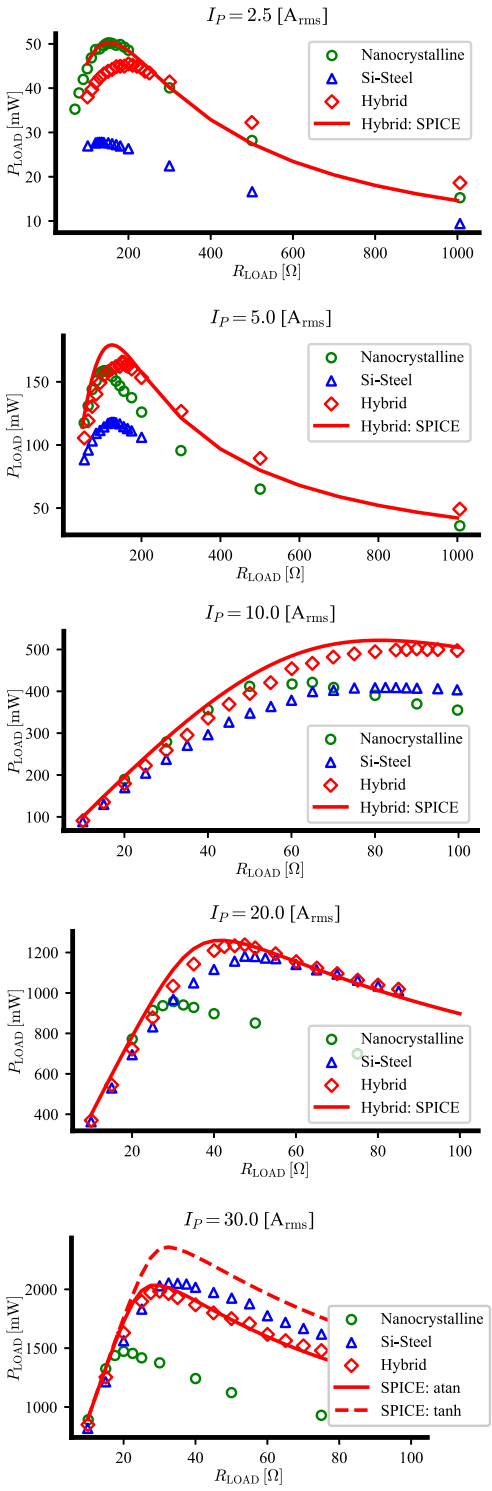

Fig. 11. SPICE-modeling of the hybrid CTMEH yields strong agreement with experimental data over a wide range of primary currents.

SPICE simulation with its nominal μ_{eff1} and μ_{eff2} values and 3 lossy simulations that vary R_{CORE} and the nominal μ_{eff1} and μ_{eff2} values $\pm 20\%$. Generally, an equivalent core loss resistance is calculated as

$$R_{\text{CORE}} = \frac{v_{\text{rms}}^2}{P_{\text{LOSS}}} \tag{13}$$

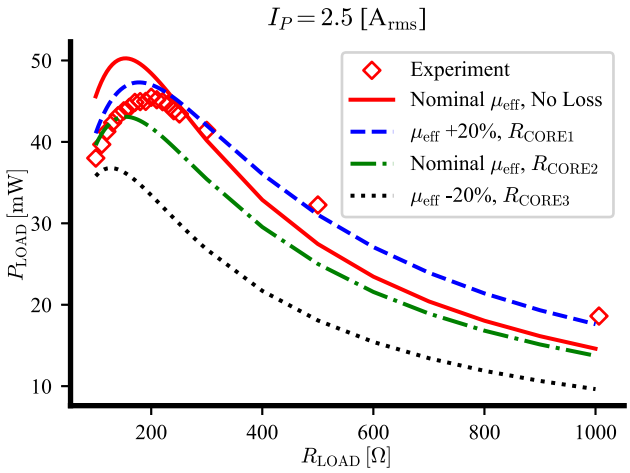

Fig. 12. Modeling core loss and refining the highly sensitive μ_{eff} parameters of the hybrid core SPICE model yield stronger agreement with experimental observations. ($R_{\text{CORE1}} = 800\,\Omega$, $R_{\text{CORE2}} = 1000\,\Omega$, $R_{\text{CORE3}} = 1200\,\Omega$).

where v_{rms} is the rms voltage across the secondary winding and P_{LOSS} is the total core loss. We estimated P_{LOSS} values from core loss density measurements and Steinmetz equations in existing specification sheets of nanocrystalline [23] and silicon steel cores [24]. Existing literature has proposed a method of approximating a rectangular hysteresis curve for very high permeability harvester cores and using a numerical solver to recalculate an accurate R_{CORE} for each R_{LOAD} value (i.e. each rms secondary voltage value) along the resistive load sweep [4]. Here, we calculate a single R_{CORE} at a nominal peak saturation flux density of 1.0T to capture good accuracy over the unsaturated, soft saturated, and hard saturated regimes with a single R_{CORE} parameter value used throughout the entire R_{LOAD} sweep. For the 2.5A$_{\text{rms}}$ test, the experimental rms output voltage on the core secondary ranged from about 2V$_{\text{rms}}$ to 4V$_{\text{rms}}$, and thus $v_{\text{rms}} \approx 3$ V$_{\text{rms}}$ was used as a nominal value for calculating R_{CORE}. Based on our P_{LOSS} estimates, the equivalent R_{CORE} for the si-steel portion of the hybrid core was approximately 268 Ω, and the equivalent R_{CORE} for the nanocrystalline portion of the hybrid core was approximately 1471 Ω. The three core loss resistances used in the refined SPICE modeling span values selected within this range. Fig. 12 demonstrates that some nonzero core loss and refinement of the μ_{eff} estimates yields close agreement between the SPICE modeling and the hybrid experimental power harvest at the low 2.5A$_{\text{rms}}$ primary current. The 20%-"inflated" μ_{eff} values with an equivalent core loss resistance of 800 Ω appear to produce the strongest agreement with the experimental data.

B. *Optimal Loading*

It is interesting to also note the behavior of the "optimal" load conditions for each harvester over the wide primary current sweep. The "optimal R_{LOAD}" is the resistive load value at which P_{LOAD} was maximized. Fig. 13 displays the experimental optimal R_{LOAD} values (at which $P_{\text{LOAD}} = P_{\text{MAX}}$) for each harvester assembly at each primary current excitation. Fig. 13 highlights that, not only do the optimal R_{LOAD} conditions vary between the nanocrystalline, si-steel, and hybrid cores at

TABLE III
EXPERIMENTAL PERFORMANCE COMPARISON OF RECENT CTMEHS

Ref.	[7]	[8]	[10]	[11]	[17]	**This Work**				
Core Type	Split	Ungapped	Cascaded (Split, Ungapped)	Ungapped	Split	Split				
Core Material	Si-Steel	Nanocrystalline (VITROPERM)	Nanocrystalline (VITROPERM)	Nanocrystalline (Fullstar No.312)	Si-Steel	Hybrid				
Core Volume [cm^3]	192	2.3	212 (Split) 8.8 (Ungapped)	12.1	216	21.4				
Primary Turns	1	1	2 (Split) 50 (Ungapped)	1	1	1				
Secondary Turns	30	200	78 (Split) 108 (Ungapped)	100	55	100				
Primary Current [A_{rms}]@[Hz]	250 A_{rms} @ 50Hz	4.0 A_{rms} @ 60Hz	8.0 A_{rms} @ 50Hz	10.0 A_{rms} @ 50Hz	350 A_{rms} @ 50Hz	2.5 A_{rms} @ 60Hz	5.0 A_{rms} @ 60Hz	10.0 A_{rms} @ 60Hz	20.0 A_{rms} @ 60Hz	30.0 A_{rms} @ 60Hz
Harvest Enhancement Strategy	N/A	Transfer Window Alignment	Desaturation (Crisscross Switches)	Desaturation (Control Winding)	N/A	N/A	N/A	N/A	N/A	N/A
Max Avg. Power Harvest [mW]	173000	42.70	848	283	205240	45.481	165.57	501.36	1238.1	1983.8
Max Avg. Power Harvest Density [$\frac{mW}{(cm^3\ A_{rms}T}$]	3.6	4.6	0.24	2.34	2.71	0.850	1.55	2.34	2.89	3.09

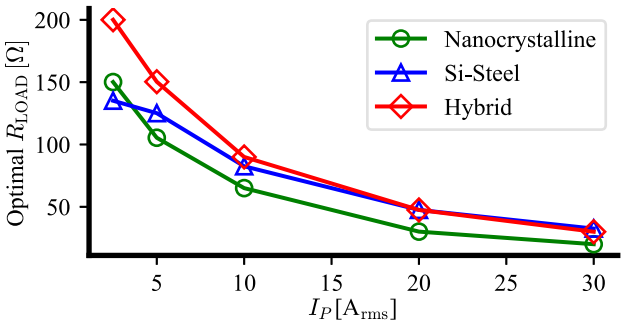

Fig. 13. Optimal loading for maximum power harvest varies across core materials and primary current conditions.

a given primary current level, but also the optimal R_{LOAD} for every core varies significantly as a function of primary current excitation. Moreover, the optimal R_{LOAD} grows smaller with larger primary currents. This trend is exhibited because higher primary currents more aggressively drive each harvester into an optimal soft saturation for maximum power harvest at smaller loads on the secondary winding. Conversely, this trend occurs because, at lower primary currents, larger resistive loads on the harvester secondary winding are required to drive the core into soft saturation for maximum power harvest.

C. Comparison to Related Work

Table III summarizes the experimental maximum average power harvest and operating conditions of this article's proposed hybrid core with that of state-of-the-art CTMEHs in the existing literature. The comparison presents experimentally-recorded harvester output power of recent CTMEH demonstrations that vary in terms of core configuration and type, core material, primary current conditions, and energy harvest enhancement circuits and strategies. The maximum average power harvest density metric in the final row is calculated by dividing the maximum experimentally-demonstrated power harvest of each work by the core volume and the ampere-turns of the primary winding. It is important to note that this maximum average power harvest density is a common and useful, but limited metric in comparing CTMEH performance. This is because, as discussed in Section III above, P_{MAX} does not exhibit a constant scaling relationship with I_P for a CTMEH. Depending on the range of primary currents and the harvester material, maximum power harvest scales somewhere between quadratically and linearly with I_P with a nonconstant scaling relationship over the wide primary current range evaluated in this article. Furthermore, some energy harvest enhancement strategies, such as the desaturation method from [10], yield power harvest that scales quadratically with I_P. These qualifying comments underscore the importance of evaluating each maximum average power harvest density metric in context, as simply multiplying this metric by a different core volume and a new I_P does not necessarily yield an accurate predicted P_{MAX} due to this complex scaling relationship. Each core type across references differs in its installation intrusiveness, complexity, and versatility across primary current operating conditions. The prime benefit of the hybrid harvester is its strong harvesting performance over a very wide range of primary currents, where single-material harvesters excel only in limited operating regions within this wide range.

IV. CONCLUSION

This article presented a novel, multicore current transformer magnetic energy harvester. This hybrid energy harvester, built from an assembly of concentric split toroids, leverages the high permeability of nanocrystalline alloys and the high saturation flux density of silicon steel to yield large average power harvests over a wide range of primary current conditions. A nonlinear flux linkage model that describes the saturating behavior of the multimaterial harvester is derived from Maxwell's equations, implemented in SPICE, and verified against experimental datasets in unsaturated, soft saturated, and hard saturated harvester core conditions. Results demonstrate that, under many primary current conditions, the hybrid harvester is capable of harvesting more average power than either a purely nanocrystalline or purely silicon steel core of equal volume and geometry. In contrast to the many electronic control techniques proposed for

increasing the power harvest of a given magnetic core, a hybrid multicore design presents a passive, harvester-focused solution to enhance power harvest and performance. Augmenting a hybrid core with harvester enhancing circuits, such as a series flux-shaping capacitor [8], parallel resonant capacitor [12], or more sophisticated energy harvest enhancement control algorithms, is an exciting avenue for future research.

APPENDIX

TABLE IV
SPICE PARAMETERS FOR SECTION II-C

	Nanocrystalline	Si-Steel	Hybrid 1	Hybrid 2
μ_{eff1} [unitless]	25000	10000	10000	25000
B_{SAT1} [T]	1.2	2.0	2.0	1.2
μ_{eff2} [unitless]	25000	10000	25000	10000
B_{SAT2} [T]	1.2	2.0	1.2	2.0
r_0 [mm]	9			
r_1 [mm]	14			
r_2 [mm]	16			
r_3 [mm]	21			
h [mm]	20			
N [Turns]	100			

ACKNOWLEDGMENT

The authors would like to thank Khang Le for his valuable contributions to the magnetic core experimental rig.

REFERENCES

[1] J. Jeong, M. Shim, J. Maeng, I. Park, and C. Kim, "An efficiency-aware cooperative multicharger system for photovoltaic energy harvesting achieving 14% efficiency improvement," *IEEE Trans. Power Electron.*, vol. 35, no. 3, pp. 2253–2256, Mar. 2020.

[2] Y. K. Tan and S. K. Panda, "Optimized wind energy harvesting system using resistance emulator and active rectifier for wireless sensor nodes," *IEEE Trans. Power Electron.*, vol. 26, no. 1, pp. 38–50, Jan. 2011.

[3] B. Zhao, J. Wang, W.-H. Liao, and J. Liang, "A bidirectional energy conversion circuit toward multifunctional piezoelectric energy harvesting and vibration excitation purposes," *IEEE Trans. Power Electron.*, vol. 36, no. 11, pp. 12 889–12897, Nov. 2021.

[4] J. Moon and S. B. Leeb, "Analysis model for magnetic energy harvesters," *IEEE Trans. Power Electron.*, vol. 30, no. 8, pp. 4302–4311, Aug. 2015.

[5] M. Gao, L. Yi, and J. Moon, "Mathematical modeling and validation of saturating and clampable cascaded magnetics for magnetic energy harvesting," *IEEE Trans. Power Electron.*, vol. 38, no. 3, pp. 3455–3468, Mar. 2023.

[6] D. Monagle, E. Ponce, and S. B. Leeb, "Generalized analysis method for magnetic energy harvesters," *IEEE Trans. Power Electron.*, vol. 37, no. 12, pp. 15764–15773, Dec. 2022.

[7] A. Abramovitz, M. Shvartsas, and A. Kuperman, "On the maximum power of passive magnetic energy harvesters feeding constant voltage loads under high primary currents," *IEEE Trans. Power Electron.*, vol. 39, no. 10, pp. 12076–120 80, Oct. 2024.

[8] J. Moon and S. B. Leeb, "Power electronic circuits for magnetic energy harvesters," *IEEE Trans. Power Electron.*, vol. 31, no. 1, pp. 270–279, Jan. 2016.

[9] D. Monagle, E. A. Ponce, and S. B. Leeb, "Rule the joule: An energy management design guide for self-powered sensors," *IEEE Sensors J.*, vol. 24, no. 1, pp. 6–15, Jan. 2024.

[10] M. Gao, L. Yi, and J. Moon, "Intracycle gapless core desaturation via crisscross switches for maximal magnetic energy harvesting," *IEEE Trans. Ind. Electron.*, vol. 72, no. 3, pp. 2476–2486, Mar. 2025.

[11] Y. Zhuang et al., "Improving current transformer-based energy extraction from ac power lines by manipulating magnetic field," *IEEE Trans. Ind. Electron.*, vol. 67, no. 11, pp. 9471–9479, Nov. 2020.

[12] D. Monagle, E. Ponce, and S. B. Leeb, "Resonant circuits for split-core magnetic energy harvesters," *IEEE Trans. Ind. Electron.*, vol. 71, no. 8, pp. 9932–9941, Aug. 2024.

[13] Z. Liu, Y. Li, Z. Hu, Z. Zang, X. Wen, and Z. He, "A wide-range self-powered current measurement method based on induced current multiplexing for online monitoring devices in transmission lines," in *IEEE Trans. Circuits Syst. I: Reg. Papers*, vol. 72, no. 3, pp. 1486–1494, Mar. 2025.

[14] S. Paul, S. Bashir, and J. Chang, "Design of a novel electromagnetic energy harvester with dual core for deicing device of transmission lines," in *IEEE Trans. Magn.*, vol. 55, no. 2, 2019, Art. no. 8000104.

[15] W. Wang, C. Xu, C. Zhang, and C. Chen, "Start-up and saturation optimization of high-power energy harvester with compound topologies overhead ac transmission line," *IEEE Trans. Emerg. Sel. Topics Power Electron.*, vol. 8, no. 4, pp. 3609–3617, Dec. 2020.

[16] J. Moon, J. Donnal, J. Paris, and S. B. Leeb, "Vampire: A magnetically self-powered sensor node capable of wireless transmission," in *Proc. 28 Annu. IEEE Appl. Power Electron. Conf. Expo.*, 2013, pp. 3151–3159.

[17] A. Kuperman, "Optimal load type for passive magnetic energy harvesters," *IEEE Sens. Lett.*, vol. 9, no. 4, Apr. 2025, Art. no. 2501604.

[18] Y. Siton, A. Abramovitz, M. Shvartsas, M. Sitbon, G. I. Orfanoudakis, and A. Kuperman, "Efficiency of passive magnetic energy harvesters operating under high primary currents," in *Proc. IEEE 21st Int. Power Electron. Motion Control Conf.*, 2024, pp. 1–5.

[19] C. Tan, Y. Zhao, and Z. Tang, "Study on energy harvesting of open-close current transformer," in *Proc. Int. Conf. Sens. Meas. Data Analytics Era Artif. Intell.*, 2020, pp. 567–571.

[20] W. Zhou, Z. Liu, Q. Huang, Y. Jiang, and Z. Cong, "Design of magnetic cores for current transformer energy harvesting devices," in *Proc. IEEE PES Asia-Pacific Power Energy Eng. Conf.*, 2019, pp. 1–5.

[21] K. Draxler, J. Hlavaček, R. Prochazka, M. Knenicky, and R. Styblikova, "Clamp current transformers for noninvasive calibration of current transformers," in *Proc. IEEE Int. Instrum. Meas. Technol. Conf.*, 2016, pp. 1–6.

[22] C. W. T. McLyman, *Transformer and Inductor Design Handbook*, 3rd ed. New York, NY, USA: Marcel Dekker Inc., 2004.

[23] "Nanocrystalline Material (FINEMET)," U. S. Department of Energy - National Energy Technology Laboratory, Sep. 2018. [Online]. Available: https://www.netl.doe.gov/sites/default/files/netl-file/Core-Loss-Datasheet-Nano-crystalline%5B1%5D.pdf

[24] "3% Silicon steel core material (grain-oriented electrical steel)," U.S. Department of Energy - National Energy Technology Laboratory, Sep. 2018. [Online]. Av.ailable: https://www.netl.doe.gov/sites/default/files/netl-file/Core-Loss-Datasheet-3-percent%5B1%5D.pdf

[25] T. Chailloux, M.-A. Raulet, C. Martin, C. Joubert, F. Sixdenier, and L. Morel, "Magnetic behavior representation taking into account the temperature of a magnetic nanocrystalline material," *IEEE Trans. Magn.*, vol. 48, no. 2, pp. 455–458, Feb. 2012.

[26] G. Goldbeck, G. Bramerdorfer, W. Amrhein, J. Hinterdorfer, and B. Weiß, "Modeling of the temperature dependence of soft magnetic materials," in *Proc. IEEE Energy Convers. Congr. Expo.*, 2020, pp. 1067–1074.

[27] Nanocrystalline/Silicon Steel (CRGO) Cut Core, Guangzhou Amorphous Electronic Technology Co. Ltd., Accessed: 2025. [Online]. Available: https://www.coilcore.com/nanocrystalline-silicon-steel-crgo-cut-core_p10.html

Daniel Monagle (Graduate Student Member, IEEE) received the B.S. degree in electrical engineering in 2020 and the S.M. degree in computer science in 2022 from the Massachusetts Institute of Technology, Cambridge, MA, USA, respectively, where he is currently working toward the the Ph.D. degree in electrical engineering and computer science.

His research interests include energy harvesting, magnetics, low-power circuit design, and self-powered systems.

Mr. Monagle was the recipient of the MIT School of Engineering 2023-2024 Thomas G. Stockham Jr. Fellowship for excellence in teaching and mentoring and the IEEE Sensors Journal 2025 Best Paper Award.

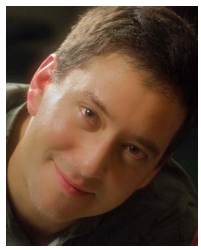

Steven B. Leeb (Fellow, IEEE) received the Ph.D. degree from the Massachusetts Institute of Technology, Cambridge, MA, USA, in 1993.

He has served as a Commissioned Officer in the USAF reserves, and he has been a Member of the MIT Faculty with the Department of Electrical Engineering and Computer Science, since 1993. He also holds a joint appointment in MIT's Department of Mechanical Engineering. He authored or coauthored more than 200 publications and 20 U.S. Patents in the fields of electromechanics and power electronics.